Article

Interaction of Nitrite Ions with Hydrated Portlandite Surfaces: Atomistic Computer Simulation Study

Evgeny V. Tararushkin [1], Vasily V. Pisarev [1,2] and Andrey G. Kalinichev [3,*]

[1] International Laboratory for Supercomputer Atomistic Modelling and Multi-Scale Analysis, HSE University, 101000 Moscow, Russia; etararushkin@hse.ru (E.V.T.); vpisarev@hse.ru (V.V.P.)
[2] Joint Institute for High Temperatures of the Russian Academy of Sciences, 125412 Moscow, Russia
[3] Laboratoire SUBATECH, UMR 6457–Institut Mines Télécom Atlantique, Nantes Université, CNRS/IN2P3, 44307 Nantes, France
[*] Correspondence: kalinich@subatech.in2p3.fr

Abstract: The nitrite admixtures in cement and concrete are used as corrosion inhibitors for steel reinforcement and also as anti-freezing agents. The characterization of the protective properties should account for the decrease in the concentration of free NO_2^- ions in the pores of cement concretes due to their adsorption. Here we applied the classical molecular dynamics computer simulation approach to quantitatively study the molecular scale mechanisms of nitrite adsorption from $NaNO_2$ aqueous solution on a portlandite surface. We used a new parameterization to model the hydrated NO_2^- ions in combination with the recently upgraded ClayFF force field (ClayFF-MOH) for the structure of portlandite. The new NO_2^- parameterization makes it possible to reproduce the properties of hydrated NO_2^- ions in good agreement with experimental data. In addition, the ClayFF-MOH model improves the description of the portlandite structure by explicitly taking into account the bending of Ca-O-H angles in the crystal and on its surface. The simulations showed that despite the formation of a well-structured water layer on the portlandite (001) crystal surface, NO_2^- ions can be strongly adsorbed. The nitrite adsorption is primarily due to the formation of hydrogen bonds between the structural hydroxyls on the portlandite surface and both the nitrogen and oxygen atoms of the NO_2^- ions. Due to that, the ions do not form surface adsorption complexes with a single well-defined structure but can assume various local coordinations. However, in all cases, the adsorbed ions did not show significant surface diffusional mobility. Moreover, we demonstrated that the nitrite ions can be adsorbed both near the previously-adsorbed hydrated Na^+ ions as surface ion pairs, but also separately from the cations.

Keywords: portlandite; hydration; nitrite; NO_2^-; adsorption; hydrogen bonding; molecular dynamics simulation

1. Introduction

Cement-based concretes are capillary-porous materials that are often exposed to an aggressive environment (sulfate and chlorine attacks, alkali–aggregate expansion reactions, etc.). This can detrimentally affect the durability of structures made of concrete and reinforced concrete. To increase their durability and sustainability, various chemical additives are used. The application of such chemical additives is one of the effective solutions to green chemistry in concrete production [1]. Calcium and sodium nitrites, $Ca(NO_2)_2$ and $NaNO_2$, are important chemical admixtures in the manufacture of concretes based on Portland cement. They inhibit the corrosion of reinforcing steel in reinforced concrete [2,3] and also act as anti-freezing agents [4,5]. It has been found that the nitrite ions, NO_2^-, bind to the cement surfaces [6]. This process reduces the concentration of free hydrated NO_2^- in aqueous solutions inside concrete pores, thus reducing the effect of corrosion inhibition in the presence of Cl^- ions. Therefore, molecular scale understanding of the hydrated NO_2^-

behavior at the surfaces of cementitious materials is important for reliable prediction of the durability of reinforced concrete structures.

Portlandite, Ca(OH)$_2$, is one of the important mineral phases of hydrated Portland cement, which is involved in the formation of the crystalline framework of hardened cement. The presence of portlandite maintains the high pH of the hardened cement [7], which is another factor protecting the reinforcing steel from corrosion [8]. In this paper, we chose this crystalline phase of hardened cement to quantify, by means of classical atomistic simulations, the structural, dynamic, and energetic aspects of its interactions with nitrite ions. According to experimental data [6], the use of the Ca(NO$_2$)$_2$ admixture can lead to the formation of new Ca(OH)$_2$ crystals on the surface of existing portlandite crystals. This might introduce some undesirable ambiguity into the definition and quantitative analysis of the portlandite-solution interface within our current molecular modeling approaches. Therefore, NaNO$_2$ rather than Ca(NO$_2$)$_2$ was selected for our simulations as a model nitrite admixture.

Methods of atomistic computer simulations make it possible to obtain detailed quantitative information about the adsorption and binding of ions on various surfaces at a fundamental molecular scale. In recent years, they have increasingly become an important and powerful tool in cement research [9–11]. The methods of atomistic computational modeling can be roughly subdivided into deterministic and stochastic. The stochastic approach of Monte Carlo (MC) simulations offers a statistical–mechanical description of materials, which is most useful for studying various thermodynamic characteristics, the energetics of adsorption, and other equilibrium properties of the simulated system under given thermodynamic conditions [12,13]. The deterministic approaches of molecular dynamics (MD) are based on the numerical solution of a set of Newtonian equations of motion for a large number of interacting particles (atoms, molecules, ions). In addition to thermodynamic properties, the MD approach also allows the calculation of many important dynamic properties, such as transport coefficients, vibrational spectra, or various relaxation times in the simulated system [14,15]. In the present work, we employed the method of classical MD simulations to model portlandite and its interaction with an interfacial aqueous solution of sodium nitrite. The recently modified version of the ClayFF force field (ClayFF-MOH) [16] with explicit Metal-O-H (MOH) angular bending terms [17] was used to simulate portlandite, while for the hydrated NO$_2{}^-$ ions a new parametrization of intermolecular interaction constants was recently developed [18]. Recent molecular simulations of the interfaces between aqueous salt solutions and another significant cement phase of ettringite [19] have already clearly demonstrated the importance of the MOH terms for accurate modeling of the mineral systems containing structural and interfacial hydroxyl groups. In addition to a more accurate reproduction of the properties of hydroxide minerals themselves, the introduction of MOH terms also affects the structural and dynamic properties of aqueous solutions in the near-surface layers of solutions compared to the original version of the ClayFF force field [20,21].

## 2. Models and Methods

2.1. Structural Models

Portlandite belongs to the group of metal hydroxides; M(OH)$_2$ (M stands for a divalent metal cation), and has a brucite-like layered structure. Portlandite crystals have $P\bar{3}m1$ symmetry and the crystal structure consists of alternating trioctahedral layers along the *c*-axis that terminate with hydroxyl groups. The layers are formed by distorted edge-sharing CaO$_6$ octahedra, with each hydroxyl ion being linked to three calcium ions [22,23].

An ideal unit cell of portlandite used in this work was built according to the structure determination by neutron diffraction measurements [24] with the lattice parameters of a = 3.59 Å, c = 4.90 Å, γ = 120°. A supercell of 10 × 10 × 8 unit cells along the *a*, *b*, and *c* cell vectors, respectively, was constructed for our simulations. The supercell had dimensions of approximately 35.9 × 35.9 × 39.3 Å^3 and contained 4000 atoms.

To simulate the interface of portlandite with $NaNO_2$ aqueous solution, a system consisting of $11 \times 10 \times 8$ portlandite unit cells was cleaved parallel to the (001) plane and cut in the ab plane of the crystal to a rectangular shape. The (001) interface orientation is chosen because it has one of the lowest cleavage-free energies of all possible portlandite crystal faces [25–28]. Despite its hydrophilicity, the (001) crystal surface is more resistant to dissolution in water compared to other crystal faces of portlandite and brucite [29–31].

The created portlandite surfaces were brought into contact with a layer of $NaNO_2$ aqueous solution approximately 85 Å thick. According to experimental data [32], this size is comparable to typical capillary pores in hardened cement. After the insertion of the aqueous layer, the dimensions of the simulation supercell were ~$71.7 \times 62.1 \times 122.8$ Å^3. The number of H_2O molecules in the nanopore corresponded to the density of the aqueous solution under ambient conditions (≈ 1 g/cm^3). The Na^+ and $NO_2{}^-$ ions were initially uniformly distributed in the nanopore. The resulting nominal $NaNO_2$ solution molality in the pore space was ≈ 0.56 mol/kg (12,632 H_2O molecules and 64 ion pairs). This corresponds to the experimentally measured solution molalities in the pores in cement materials [6].

Figure 1 shows a representative snapshot fragment of the simulation supercell. For the subsequent analysis, the interfacial space occupied by the solution was subdivided into three layers. The first near-surface layer (I) starts from the average positions of hydroxyl hydrogen atoms on the portlandite surface, H_h, and has a thickness of 3.5 Å (approximately one molecular diameter of H_2O. The second layer (II) immediately follows it and has the same thickness of 3.5 Å. In the rest of the pore space (III), the solution is considered to be much less affected by the surface and has properties close to those of the bulk phase.
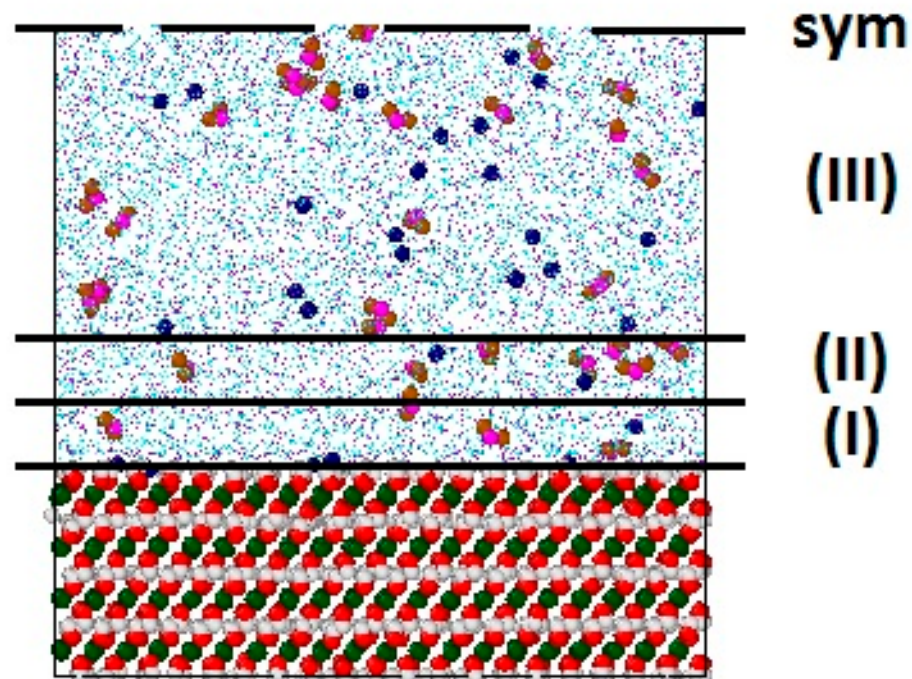
Figure 1. A representative snapshot of the simulation supercell of portlandite with $NaNO_2$ aqueous solution. The thick black lines schematically indicate the first 3.5 Å (**I**), second 3.5 Å (**II**) solution layers next to the surface, and the bulk phase (**III**). **sym** is the symmetry plane of this slit-like pore.

2.2. Force Field Parameters

A series of preliminary simulations for the bulk $Ca(OH)_2$ crystals was initially performed with both ClayFF-orig and ClayFF-MOH versions of the force field, in order to assess the relative accuracy of both versions. The MOH variation adds harmonic energy terms for Metal-O-H (M-O-H) angle bending in the crystal structure. The equilibrium angles and stiffness parameters were originally reported for Mg-O-H and Al-O-H angles [17]. They have been fitted to reproduce the lattice structure and dynamics obtained by

density functional theory (DFT) calculations of brucite (Mg(OH)$_2$)and gibbsite (Al(OH)$_3$). The optimized parameters for Mg-O-H angles are as follows [16]: $\theta_{0,MgOH} = 110°$ and $k_{MgOH} = 6$ kcal·mol^{-1}·rad^{-2}. In this work, we use the same parameters for the Ca-O-H angles, based on the close similarity between the Mg(OH)$_2$ and Ca(OH)$_2$ crystal structures.

Water molecules were modeled using the flexible SPC/E model [33], and the parameters representing hydrated Na$^+$ ions were taken from the updated ClayFF model [16]. As mentioned above, we used here a new parameterization of charges, Lennard-Jones constants, and intramolecular constants for the NO$_2^-$ ions in combination with the ClayFF force field [18]. This parameterization took into account recent results of DFT calculations for the nitrite ion dissolved in water [34,35], some earlier NO$_2^-$ models use in classical MD simulations [36–38], and experimental data [39]. All force field parameters used in this work were specifically parametrized to be consistent with the same SPC/E water model, therefore they are expected to be transferable and provide reliable results in the simulations of other systems that are consistent with the same model of water, as has been already demonstrated numerous times in the ClayFF-based simulations of various nanoporous and layered materials and their aqueous interfaces over the last 20 years [16].

2.3. Simulation Details

All MD simulations were performed using the LAMMPS simulation package [40]. LAMMPS is one of the most commonly used computer simulation software packages for modeling of cementitious materials and their interfaces with aqueous solutions (e.g., ref. [11]). Periodic boundary conditions in all three dimensions were used in all simulations. A cutoff radius of 12.5 Å was used for short-range forces, and the PPPM method was used to account for long-range electrostatic interactions [41,42]. The GPU accelerator within the LAMMPS package was used to speed up the calculations [42,43]. Standard Lorentz-Berthelot mixing rules ($\varepsilon_{ij} = \sqrt{\varepsilon_{ii}\varepsilon_{jj}}$; $\sigma_{ij} = (\sigma_{ii} + \sigma_{jj})/2$) were applied to calculate the Lennard-Jones parameters of interaction between unlike atoms [16,41]. The Newtonian equations of motion were numerically integrated with a time step of 0.5 fs via the velocity–Verlet algorithm [41,44].

The constructed models were initially equilibrated for 1 ns at the temperature of 298 K and pressure of 1 bar using the Nose-Hoover thermo-barostat [41,45,46]. After the equilibration in the *NPT* statistical ensemble (constant number of particles, constant temperature, and constant pressure), the equilibrium simulation run was performed in the *NVT* statistical ensemble (constant number of particles, constant temperature, and constant volume) using the Nose-Hoover thermostat [41,45,46]. The equilibrium *NVT* part was also 1.0 ns long and the generated equilibrium dynamic trajectories of atoms were then used for further statistical analysis.

The quantitative analysis of the structure, dynamics, and energetics of the portlandite-solution interfaces was performed following the standard approaches that are commonly used for such kinds of interfacial simulations (e.g., ref. [47]).

3. Results and Discussion
3.1. Bulk Portlandite Properties
#### 3.1.1. Crystallographic and Structural Parameters

Table 1 shows the equilibrium parameters of the crystallographic unit cell of portlandite calculated with the ClayFF-orig and ClayFF-MOH versions of the force field, in comparison with experimental data [24,48], DFT calculations [26,49,50], and earlier results of classical MD simulations [11,51–54]. In our simulations, all unit cell parameters were optimized in the NPT ensemble MD runs without any symmetry constraints.

Table 1. Crystallographic unit cell parameters of portlandite: simulation results and experimental data.

Source	*a*, Å	*b*, Å	*c*, Å	*α*, °	*β*, °	*γ*, °
ClayFF-orig (This work)	3.6343	3.6357	4.8957	90.05	90.00	119.99
ClayFF-MOH (This work)	3.6779	3.6783	4.8767	90.03	89.98	119.99
ClayFF [51]	3.567	3.567	4.908	90	90	120
IFF [11]	3.75	3.75	4.38	90	90	120
CementFF [11]	3.68	3.67	4.81	90	90	120
CSH-FF [52]	3.5037	3.5037	4.8045	90	90	120
ERICA FF [53]	3.67 (2.2)	3.67 (2.2)	4.85 (0.4)	89.7	89.9	120
ReaxFF [54]	3.63	3.63	5.10	89.67	90.05	120.11
DFT [49]	3.609	3.609	4.864	90	90	120
DFT [26]	3.696	3.696	5.147	90	90	120
DFT [50]	3.581–3.625	3.581–3.625	4.797–5.010	90	90	120
Neutron diffraction [24]	3.5918	3.5918	4.9063	90	90	120
NMR [48]	3.5925	3.5925	4.905	90	90	120

The results clearly reproduced the hexagonal crystal structure, in agreement with experimental data, and the discrepancy of lattice parameters did not exceed 2.4% for the ClayFF-MOH version. Both versions of the ClayFF force field also showed a good agreement with the DFT results. There were no significant differences in the crystallographic parameters between the ClayFF-orig and ClayFF-MOH models, indicating that introducing the explicit M-O-H angle bending terms in portlandite does not affect the symmetry of the crystal. One has to note, however, that this agreement is not particularly surprising because portlandite was one of the model structures used to parametrize the original ClayFF force field [20,21].

The small differences in the crystallographic parameters between the ClayFF-orig and ClayFF-MOH models are due to the much stronger localization of the hydrogen atoms and the orientation of hydroxyl groups for the latter case (Figure 2). In the case of ClayFF-orig, the hydroxyl groups are freely oriented with their hydrogen atoms, H_h, towards one of the three hydroxyl oxygen atoms, O_h, of the opposite crystal layer, forming a strong hydrogen bond. Due to the unconstrained Ca-O-H angle in the ClayFF-orig, the hydroxyl groups can frequently and freely rotate, and those hydrogen bonds switch between three O_h atoms from the opposite layer. Such poorly constrained rotations of hydroxyl groups lead to a slight expansion of the interlayer space. Consequently, the parameter *c* of the portlandite unit cell increased, and the parameters *a* and *b* decreased compared to the ClayFF-MOH. As Figure 2a shows, the H_h atoms in the ClayFF-orig model can be oriented with equal probability in all three directions, corresponding to the locations of the O_h atoms in the neighboring layer (O_h atoms of the opposite layer are not shown).

(a)   (b)
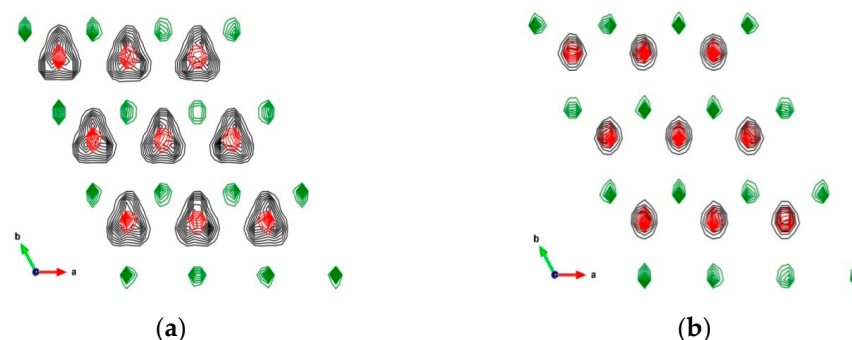
Figure 2. Time-averaged atomic density distributions of the layer of portlandite (supercell fragment from 3 × 3 unit cells). Green contours—Ca; red contours—O_h; black contours—H_h. (**a**) ClayFF-orig; (**b**) ClayFF-MOH.

Figure 2b demonstrates a much stronger localization of H_h atoms in the ClayFF-MOH model. Figure 3 shows the distributions of angles of hydroxyl groups to the *ab* plane in the original and ClayFF-MOH versions, which also reflect a more disordered behavior of hydroxyls in ClayFF-orig. In contrast, the hydroxyl O-H bonds are more strongly localized around the normal to the *ab* plane in the ClayFF-MOH model. According to the DFT results, such localized behavior of hydroxyls is more realistic of brucite-like materials [17] and is in better agreement with experimental data [22].
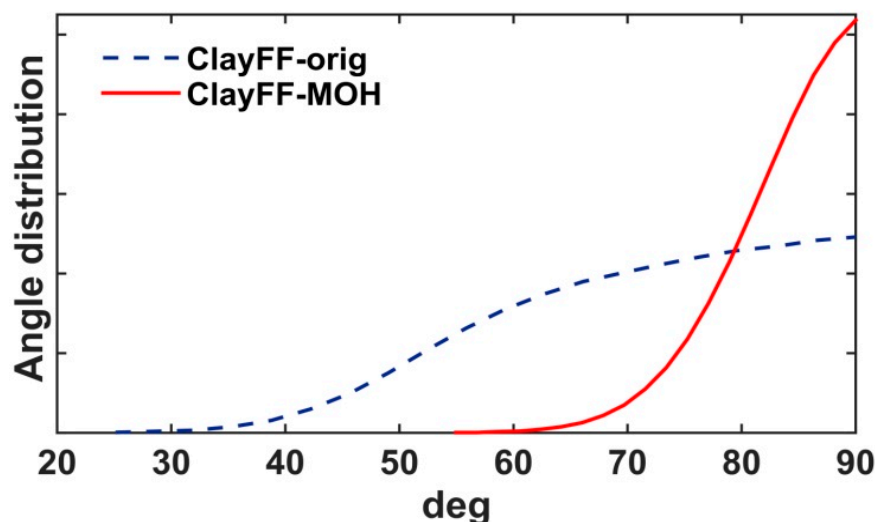

Figure 3. Hydroxyl slope angle density distributions.

3.1.2. Power Spectra of Atomic Vibrations in Portlandite Crystals

Analysis of atomic vibration spectra in the crystal gives further insights into the dynamics of portlandite hydroxyls. Figure 4 shows smoothed power spectra reflecting the vibrations in the ab crystallographic plane for all portlandite atoms and, separately, the contribution of H_h-atoms calculated in both versions of ClayFF. The smoothing of the spectra was carried out by applying the exponential damping with the characteristic time τ_{damp} = 0.25 ps to the velocity autocorrelation functions, as proposed by Szczerba et al. [55].
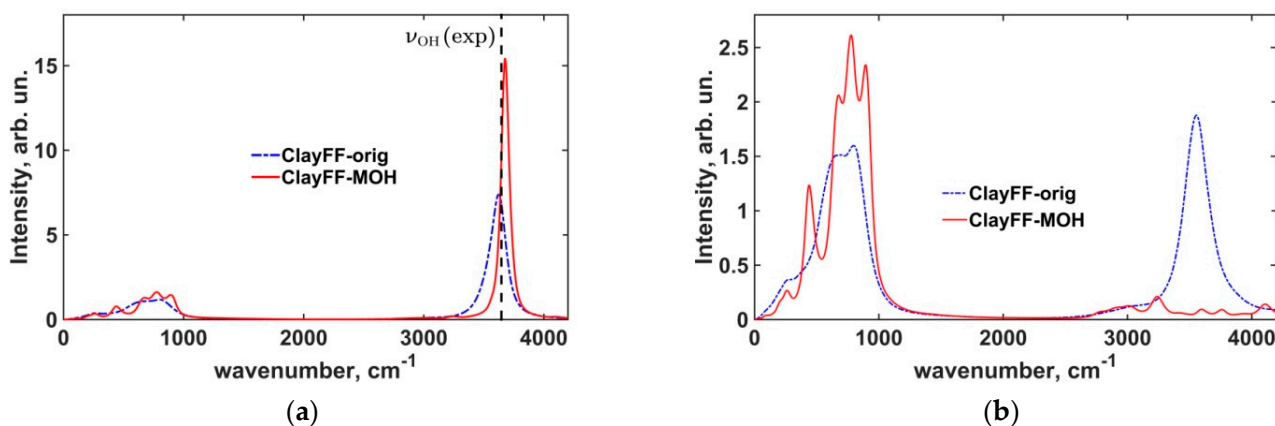

Figure 4. Power spectra of atomic vibrations. (**a**) total power spectra; (**b**) power spectra of H_h-atoms in the *ab* crystallographic plane. (exp)—see [56,57].

The low-frequency region of the spectrum corresponds to the librational modes of the hydroxyl groups and to the lattice vibrations. In the ClayFF-orig model, the individual peaks were unresolved and all merged into one single wide spectral band. In the ClayFF-MOH model, the individual peaks were better resolved for both libration and lattice

vibration modes, which is in a better qualitative agreement with the vibrational behavior of portlandite crystal observed in experiments [56] and DFT calculations [50], compared to the ClayFF-orig model.

The most noticeable differences between the two versions of ClayFF in Figure 4a,b are in the high-frequency range of the spectra. The peaks corresponding to the O–H stretching modes of hydroxyls are located at positions 3624 cm^{-1} and 3676 cm^{-1} for the ClayFF-orig and ClayFF-MOH models, respectively. For the ClayFF-MOH, the peak frequency is slightly higher than the experimental data [56–58], where the O–H stretching peaks are located at 3620 cm^{-1} (A$_{1g}$ mode) and 3646 cm^{-1} (A$_{2u}$ mode) for Raman and IR spectroscopy, respectively. The lower frequency of the O–H stretching peak in the ClayFF-orig compared to the ClayFF-MOH indicates that the interlayer hydrogen bonding is stronger in the former model. As mentioned above, in the ClayFF-orig, H$_h$ atoms instantaneously bond with only one opposite-layer O$_h$ atom. In ClayFF-MOH, an H$_h$ atom can participate in up to 3 weaker hydrogen bonds at the same time, due to the higher localization of H$_h$ atoms in the structure. For instance, in brucite under normal conditions, the preferred orientation of the hydroxyl groups is along the normal to the magnesium octahedral layer [17,59]. The reorientation of hydroxyl groups in brucite and portlandite towards the opposite-layer O$_h$ atoms occurs only at high temperatures and pressures [23,60]. This exaggerated reorientation of hydroxyls under normal conditions in the ClayFF-orig model is especially noticeable in the isolated spectrum of H$_h$-atoms in the ab crystallographic plane, where a very strong peak is observed in the high-frequency region, as seen in Figure 4b.

3.2. Properties of Portlandite-NaNO$_2$ Aqueous Solution Interfaces

3.2.1. Structural Properties of Interfacial Solutions

First, we discuss the structural differences in the simulated aqueous solution between the two ClayFF versions. Figure 5 shows atomic density profiles of H$_w$ and O$_w$ atoms of the H$_2$O molecules along the direction normal to the portlandite surface for both versions of ClayFF. As expected for the ClayFF-orig version, the profiles for H$_w$ and O$_w$ were similar to the earlier MD simulation results with this force field [20,51]. However, slightly different profiles are observed with the ClayFF-MOH model, indicating some changes in the local interfacial solution structure. Below, we argue that the reason for the changes in the density profiles in the first two solution layers, (I) and (II) (as defined in Figure 1) are directly related to very specific interfacial molecular coordinations.
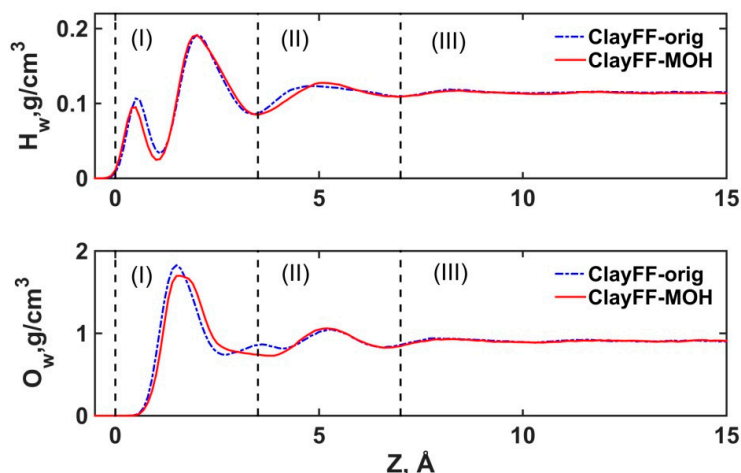
Figure 5. Atomic density distributions of H$_w$ and O$_w$ atoms for both versions of ClayFF force fields. (**I**) and (**II**) are the first and second solution layers, respectively. (**III**) denotes the bulk phase of the solution (see Figure 1).

DFT and MD results show that one of the most probable orientations of the H$_2$O molecule dipole vector is 170–175° with respect to the surface normal [26,51]. With this

orientation, the H_2O molecule donates two hydrogen bonds to the O_h atoms of the hydroxyls on the surface of the crystalline phase and this orientation of the H_2O molecule corresponds to the bidentate coordination towards the surface [55]. In addition, there may be a monodentate coordination with the dipole vector oriented $\approx 90°$ to the surface normal [55]. Such orientations of H_2O molecules on the (001) surface of portlandite have been reported in other recent MD simulations [61]. Due to the more accurately constrained vertical orientations of the surface hydroxyl groups with the ClayFF-MOH model, H_2O molecules in those two orientations are adsorbed closer to the portlandite surface. That, in turn, results in stronger hydrogen bonds in the donor-acceptor pairs $H_w \cdots O_h$ and $H_h \cdots O_w$. The stronger bonding of H_2O molecules in mono- and bidentate orientations is reflected in the shift of the first peak of the H_w profile closer to the portlandite surface (in layer (I)) compared to the ClayFF-orig version.

However, the O_w and H_w interfacial density profiles for both versions of the force field clearly reproduce the distinct layering of water at least within the first two molecular layers, which is fully consistent with the results of previous simulations [20,51,61] and justifies our definition of the solution layers in Figure 1.

The slight shift of the first minimum of the H_w profile in layer (I) for ClayFF-MOH (Figure 5) is also explained by the adsorption of the H_2O molecules closer to the portlandite surface. The second peaks of the density profiles in layer (I) are located at the same positions for both versions of the ClayFF model. These peaks are the highest and correspond to the most common orientation of H_2O molecules, in which interfacial H_2O molecules accept hydrogen bonds from surface hydroxyls (donor-acceptor pair $H_h \cdots O_w$) and H_2O molecules are located along the hydroxyl O-H bonds. In the second layer (II), the H_w density maximum shifts away from the surface for the ClayFF-MOH model compared to ClayFF-orig. The reason for this is that the mono- and bidentate-oriented H_2O molecules in layer (I) are coordinating the H_2O molecules from layer (II) in a slightly different manner due to more stable hydrogen bonds with the surface observed with the ClayFF-MOH model. These changes are reflected in the O_w profiles as well, where there are two peaks In the near-surface layer (I) and (II) for the ClayFF-MOH compared to three peaks for the ClayFF-orig. The broadening of the first peak and the absence of a peak at the boundary of layers (I) and (II) In ClayFF-MOH indicate the formation of a stronger hydrogen bonding network on the surface of portlandite. In general, the H_2O atomic density profiles for the ClayFF-MOH are qualitatively more similar to the H_2O profiles from the MD simulations with a more optimized force field for solid and a four-point TIP4P/2005 water model [61].

Thus, the ClayFF-MOH model provides a better qualitative and quantitative description of the portlandite crystal and the portlandite-water interface. Therefore, in the rest of the paper, the behavior of dissolved ions and H_2O molecules on the portlandite surface are presented and discussed only for the ClayFF-MOH model.

Figure 6 shows the density profiles of Na^+ ions and N and O_n atoms of NO_2^- in the sodium nitrite aqueous solution next to the portlandite surface. The density profile of Na^+ is similar to the previously reported profiles [20,51] with Na^+ is mainly adsorbed with inner-sphere surface coordination. Inner-sphere coordination is also observed for adsorbed NO_2^- ions, as the first density peaks of N and O_n are located within layer (I) of the solution at distances of 2.1 and 2.0 Å from H_h, respectively. The first minima of the profiles are located in both cases within the layer (II) of solution at distances of 4.0 Å for N and 4.1 Å for O_n, indicating that adsorbed NO_2^- ions can be oriented both with their N and O_n atoms towards the H_h hydroxyls. In both orientations NO_2^- ions accept hydrogen bonds from surface hydroxyls.
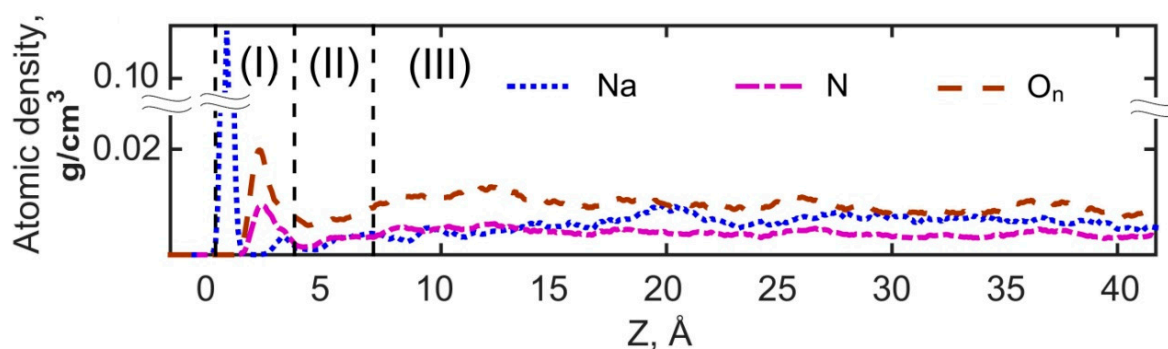
Figure 6. Atomic density distributions of Na^+ and NO_2^-. Half of the nanopore is shown due to the symmetry of the model. (**I**) and (**II**) are the first and second layers of the solution, respectively. (**III**) denotes the bulk phase of the solution (see Figure 1).

Visual analysis of the trajectories with the OVITO package [62] has shown that the adsorbed NO_2^- ions demonstrate four main types of surface coordination as illustrated in Figure 7a–d. In the first coordination (Figure 7a), all three atoms of the NO_2^- ion are in a plane oriented almost parallel to the portlandite surface and coordinated by surface hydroxyls. The other three orientations have only the N atom, one O_n atom, or both O_n atoms coordinated by the surface hydroxyls, as shown in Figures 7b, 7c and 7d, respectively. These types of coordination can be seen for the anions adsorbed next to Na^+ ions on the surface as well as for the anions located far from adsorbed cations. As mentioned above, the first minima of the N and O_n density profiles are located within the solution layer (II), so that the density of NO_2^- in that layer is lower than in layer (I) and in layer (III) that reflects bulk solution properties. This behavior of NO_2^- in layer (II) is caused by the repulsion from the first NO_2^- adsorption layer in layer (I).

(**a**)   (**b**)   (**c**)   (**d**)
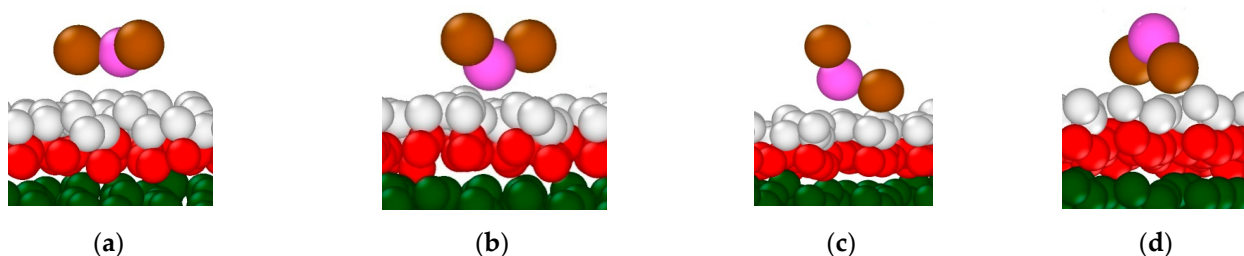
Figure 7. NO_2^- ion coordination on the portlandite surface (explanation for subfigures **a**–**d** please see Section 3.2.1 for a detailed explanation and discussion). Green sphere—Ca; red sphere—O_h; white sphere—H_h; magenta sphere—N; brown sphere—O_n.

The surface distribution of molecules visualized by atomic density contour maps for the solution layer (I) shows that Na^+ ions are adsorbed at the centers of triangles formed by O_h atoms, as illustrated in Figure 8. The inner-sphere adsorption of Na^+ ions and the coordination of the H_2O molecules around them by O_w atoms agrees well with the previous MD results [20,51]. Unlike Hu et al. [63], we did not observe the preference of NO_2^- adsorption surrounding the cations and forming surface clusters. Instead, NO_2^- ions can be adsorbed both near Na^+ and far from them. In both cases, the adsorbed anions are quite strongly bound to the surface and do not change their binding site within the time scale of the simulation. Nevertheless, the nitrite anions frequently change their orientation while staying at the same surface adsorption site. Due to the frequent changes of adsorbed NO_2^- ions orientation, the H_2O molecules that form hydrogen bonds with these NO_2^- ions did not have any predominant coordination type, as seen in Figure 8b.
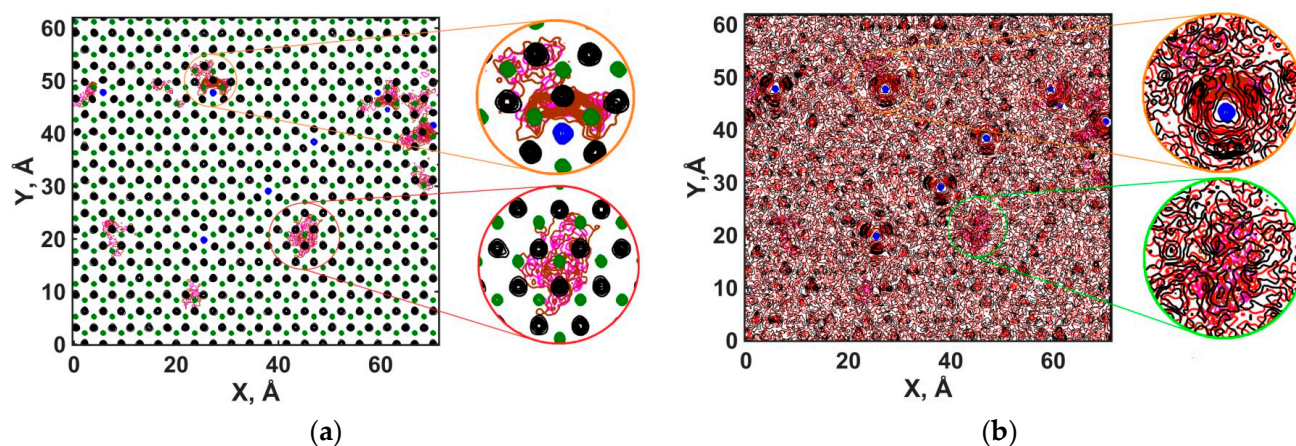
Figure 8. Contour maps of atomic density for solution species at the surface of portlandite (solution layer (I)). Green contours—Ca (**a**); black contours—H_h (**a**) and H_w (**b**); red contours—O_w (**b**); blue contours—Na^+ (**a**,**b**); purple contours—N (**a**,**b**); brown contours—O_n (**a**,**b**). (**a**) Crystalline phase and ions of an aqueous solution; (**b**) ions of an aqueous solution and atoms of H_2O molecules.

3.2.2. Power Spectra of the Interfacial Dynamics

Power spectra reflecting the vibrations of H_h atoms at the surface and in the bulk structure of portlandite are shown in Figure 9a. As mentioned in Section 3.1.2, the low-frequency region of the bulk portlandite spectrum has a band where several peaks can be resolved. In contrast to that, only two peaks can be resolved in that band for surface H_h, which indicates a superposition of normal vibration modes for surface hydroxyls. In the high-frequency range, the peak corresponding to the stretching of O–H bonds is broader, less intense, and significantly blue-shifted (3676 cm^{-1} vs. 3743 cm^{-1}) for surface hydroxyls compared to the bulk phase, which is typical for surfaces of brucite-like minerals [59]. The shift of the O–H stretching vibrations peak for surface H_h at the crystal–solution interface is significantly smaller than with the crystal-vacuum interface [59]. The reduced peak shift is due to the formation of hydrogen bonds of the surface hydroxyls with the Interfacial H_2O molecules and NO_2^- ions. Figure 9b shows that the power spectra of the H_2O solution molecules at all distances from the surface are identical. This may merely reflect the fact that simple harmonic potentials used here to model the intramolecular vibrations in the SPC/E water model are not accurate enough, and more complex inharmonic models are necessary (see, e.g., ref. [55]). However, the libration, bending, and stretching modes of H_2O molecules are reproduced with only small deviations from the experimental data [64,65].

Unlike the case with H_2O molecules, the spectra reflecting the surface dynamics of Na^+ ions show some dependence on the distance from the surface, as seen in Figure 9c, which confirms the previous MD results [20], where such spectra have been analyzed in detail. However, the NO_2^- power spectra in different solution layers have peaks at the same frequencies, differing only in magnitudes, as shown in Figure 9d. The positions of the spectral peaks are in good agreement with the results of Raman spectroscopy [39]: the calculated frequency of the bending mode, δ, is at 779 cm^{-1}, compared to 817 cm^{-1} from the Raman spectroscopy. The calculated asymmetric, ν_{as}, and symmetric, ν_s, N-O_n stretching modes peaks are at 1250 cm^{-1} and 1371 cm^{-1}, respectively, compared to the experimentally determined values of 1242 cm^{-1} and 1331 cm^{-1}.
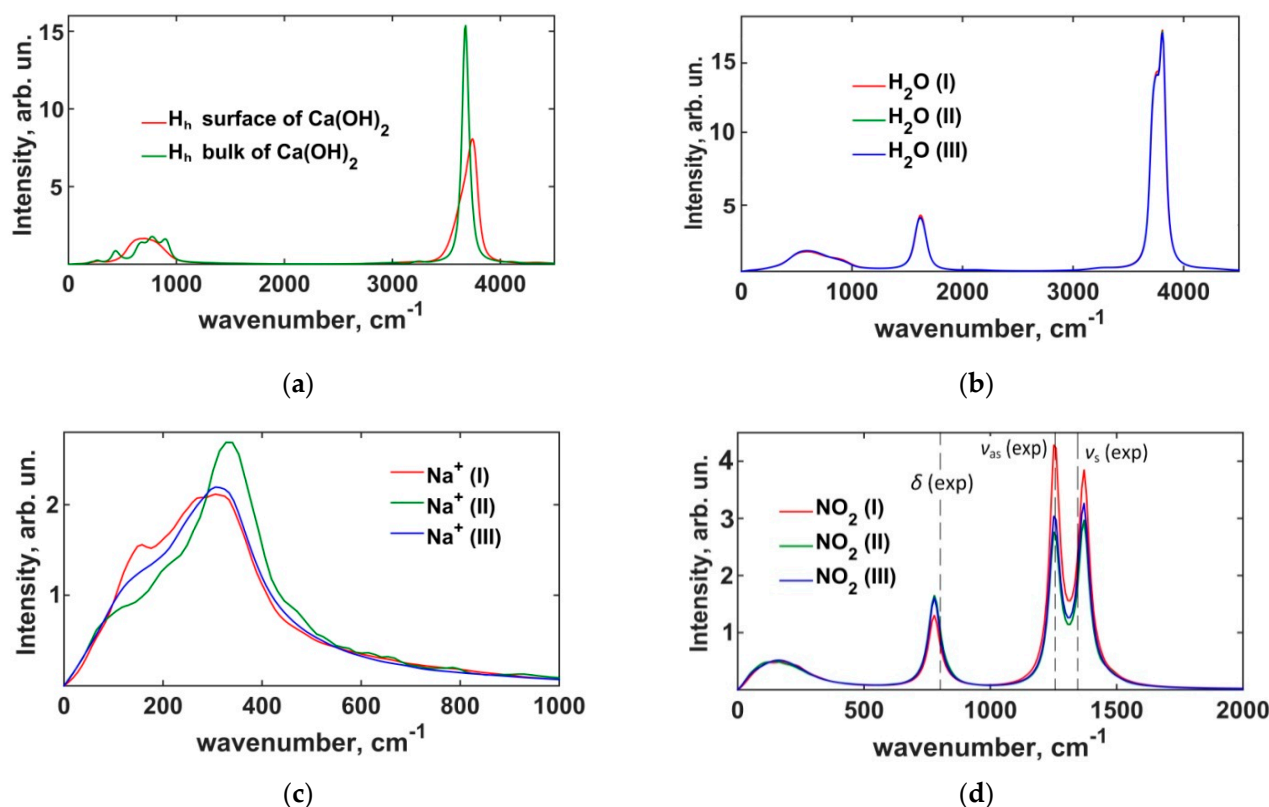
**Figure 9.** Power spectra of atomic vibrations for crystalline phase and ionic species and H_2O molecules: (**a**) H_h; (**b**) H_2O; (**c**) Na^+; (**d**) NO_2^-. (exp)—see [39]. (**I**) and (**II**) are the first and second layers of the solution, respectively. (**III**) denotes the bulk phase of the solution (see Figure 1).

3.2.3. Structure and Dynamics of the Interfacial Hydrogen Bonding

To better characterize the structural and dynamic properties of the interfacial solution, we have also studied the dynamics of hydrogen bonds (H-bonds), which were formally defined using a common geometric criterion: an H-bond between a hydrogen H_w (donor) and oxygen O_w (acceptor) atoms of two H_2O molecules was assumed to exist if the $H_w \cdots O_w$ distance is less than 2.45 Å and the angle between the H-bond direction and the vector connecting the O_w atoms of the donor and acceptor molecules is less than 30° (e.g., ref. [66]). For H-bonds between H_2O molecules and NO_2^- ($H_w \cdots N$ and $H_w \cdots O_n$ pairs), the distance thresholds were taken according to [35]: $R_{Hw-N} \leq 2.25$ Å and $R_{Hw-On} \leq 2.35$ Å. The geometrical definitions for H-bonds between portlandite surface hydroxyls and H_2O (or NO_2^-) were taken to be the same as for H_2O molecules (or H_2O and NO_2^-) in solution. The average lifetimes τ_{HB} for various types of H-bonds were then assessed by integrating the so-called continuous-time autocorrelation functions [35,66–68] as illustrated in Figure 10. In addition, the average number of hydrogen bonds n_{HB} per H_2O molecule and acceptors N and O_n were also calculated.

It was found that the portlandite hydroxyls form the most stable H-bonds with the H_2O molecules of the solution (pairs $H_h \cdots O_w$ and $H_w \cdots O_h$). The lifetime of the $H_h \cdots O_w$ bonds is longer than that for $H_w \cdots O_h$, despite the fact that in the ClayFF model, the charge of O_h is more negative than that of O_w, while the charges of H_h atoms and H_w atoms in SPC/E are almost equal. In the bidentate orientation of H_2O molecules, which is most preferable on the surface of portlandite [26], H_2O molecules are also coordinated by neighboring hydroxyls ($H_h \cdots O_w$ pairs) without forming hydrogen bonds between H_w and O_h of this hydroxyls.
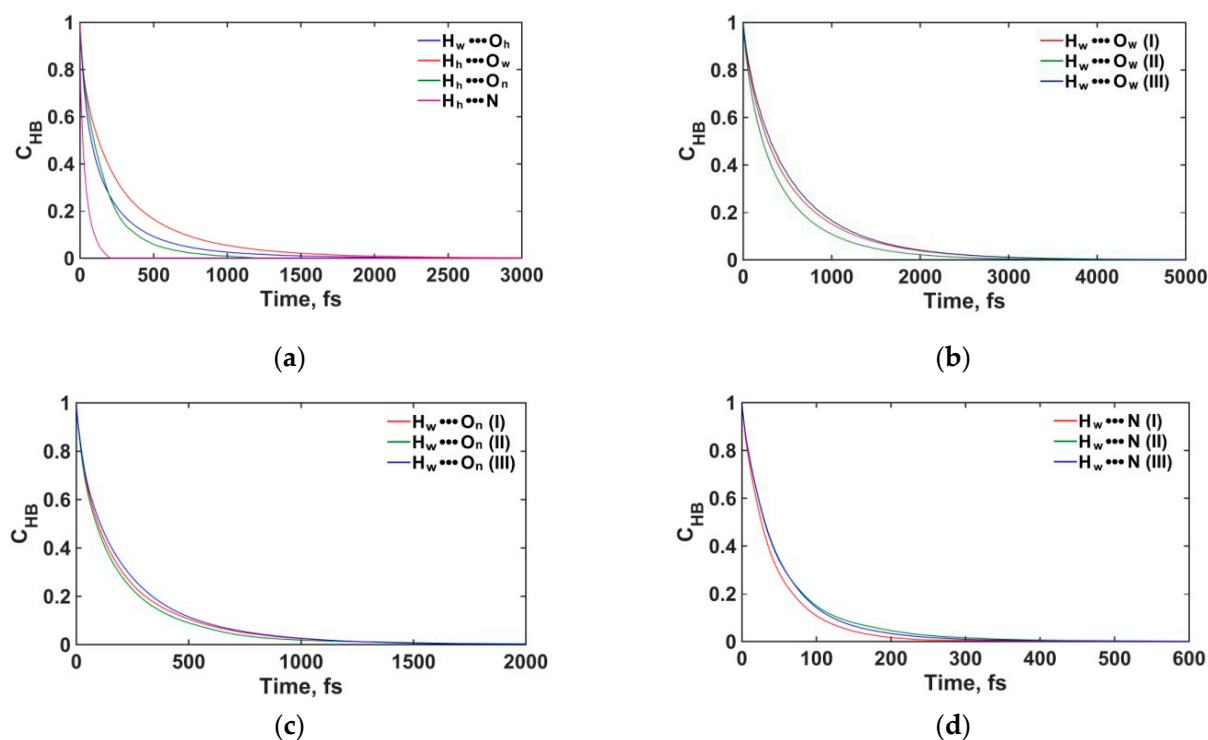
Figure 10. Continuous time autocorrelation functions. (**a**) $H_w \cdots O_h$, $H_h \cdots O_w$, $H_h \cdots O_n$, $H_h \cdots N$; (**b**) $H_w \cdots O_w$; (**c**) $H_w \cdots O_n$; (**d**) $H_w \cdots N$. (**I**) and (**II**) are the first and second layers of the solution, respectively. (**III**) denotes the bulk phase of the solution (see Figure 1).

As mentioned above, monodentate orientation can also occur, in which H-bonds between the $H_h \cdots O_w$ and $H_w \cdots O_h$ pairs are formed. Therefore, a significant role on the hydrated (001) portlandite surface is played by the H-bonds donated by the hydrogen atoms of the surface hydroxyl groups to the oxygen atoms of H_2O molecules (pair $H_h \cdots O_w$), which inhibits the penetration of H_2O molecules closer to the portlandite surface and the dissolution of calcium ions [29].

Table 2 shows that the lifetime of H-bonds between H_2O molecules in the solution layer (I) is longer than in the layer (II), while the number of H-bonds per H_2O molecule remains about the same for both near-surface layers. This means that the interaction of H_2O molecules with surface hydroxyls orients them in a way that favors the formation of a more stable H-bond network between themselves in layer (I). That H-bonding network of the H_2O molecules nearest to the surface (in layer (I)) creates an ice-like two-dimensional layer on the surface of portlandite [29]. In the bulk solution (layer (III)), the number of H-bonds per H_2O molecule and the bond lifetime have typical values for low-concentration aqueous solutions [69].

For interactions between water molecules and nitrite ions, the H-bonds $H_w \cdots O_n$ are stronger than $H_w \cdots N$, which is consistent with the DFT results for hydrated NO_2^- [35]. The H-bonds for these pairs have approximately the same lifetimes in all layers of the aqueous solution. However, the average number of H-bonds per acceptor atom in $H_w \cdots N$ pairs in layer (I) is lower than in layer (II), because some of the H_2O molecules in layer (I) bind with surface hydroxyls instead of NO_2^- nitrogen atoms. The lifetime of $H_h \cdots N$ bonds between hydroxyls and NO_2^- is close to the lifetime of the $H_w \cdots N$ bond, however, the $H_h \cdots O_n$ bonds have shorter lifetimes than $Hw \cdots On$. Such a decrease in the lifetime is due to the vibrational behavior of the surface hydroxyls of the crystalline phase, which is also noticeable when comparing the lifetimes of the $H_h \cdots O_w$ and $H_w \cdots O_w$ pairs. We can also see that the H-bonds between surface hydroxyls and adsorbed NO_2^- ions are weaker than the ones between hydroxyls and H_2O molecules. This is consistent with the absence of a strongly preferred NO_2^- orientation on the portlandite surface.

Table 2. The average number of H-bonds per H_2O molecule/acceptor (n_{HB}) and the average lifetime of H-bond (τ_{HB}).

Donor-Acceptor Pair	Layer	n_{HB}	τ_{HB}, ps
$H_w \cdots O_w$	(I)	2.26	0.51
	(II)	2.23	0.41
	(III)	3.53	0.54
$H_w \cdots O_n$	(I)	1.68	0.20
	(II)	1.67	0.18
	(III)	2.69	0.21
$H_w \cdots N$	(I)	0.89	0.04
	(II)	1.06	0.05
	(III)	1.64	0.05
$H_w \cdots O_h$	(I)	0.27	0.18
$H_h \cdots O_w$	(I)	0.43	0.27
$H_h \cdots O_n$	(I)	0.45	0.16
$H_h \cdots N$	(I)	0.20	0.04

3.2.4. Water Molecules and Nitrite Ions Orientational Relaxation

The orientational relaxation of NO_2^- ions and H_2O molecules can be characterized using the autocorrelation function of the unit vectors directed along the $N-O_n$ or O_w-H_w bonds [35,70–72], which was calculated using the second-rank Legendre polynomial:

$$C_2(\cos \theta) = \langle \frac{3}{2} \cos^2 \theta - \frac{1}{2} \rangle, \qquad (1)$$

where $\cos \theta(t) = d^T(t_0)d(t_0 + t)$ is the linear correlation between the unit vector of bond orientation d at time moments t_0 and $t_0 + t$, and angular brackets $\langle \ldots \rangle$ denote the averaging over all molecules and over all possible initial moments t_0 along the equilibrium MD trajectory. The correlation functions of NO_2^- and H_2O molecules in three layers of the aqueous solution are shown in Figure 11. The orientational correlation times were calculated by fitting C_2 with bi-exponential functions [35]:

$$C_2(t) = A_1 \exp\left(-\frac{t}{\tau_1}\right) + A_2\left(-\frac{t}{\tau_2}\right), \qquad (2)$$

where the shorter time constant τ_1 reflects the rotational inertia of an ion or molecule in the libration mode, which is affected by H-bonding around the ion/molecule [71]. The longer time constant τ_2 characterizes the reorientation of an ion or molecule due to the rotational Brownian motion and to large angular jumps associated with the breaking of H-bonds [35,71].

Table 3 shows the orientational relaxation times for NO_2^- and H_2O, depending on the molecule location in the pore. For H_2O molecules, the time τ_1 for all layers of the solution have similar values, indicating low sensitivity of librational molecular motions to the variation of local H-bonding environment between bulk solution and near-surface layers. The power spectra in Figure 9b also indicate the same behavior in the low-frequency region. On the other hand, the time τ_2 for H_2O molecules increases in the near-surface layers. Such an increase in rotational relaxation time confirms the aforementioned formation of a more stable H-bonding network at the surface of crystalline portlandite due to hydroxyl group–water interactions.
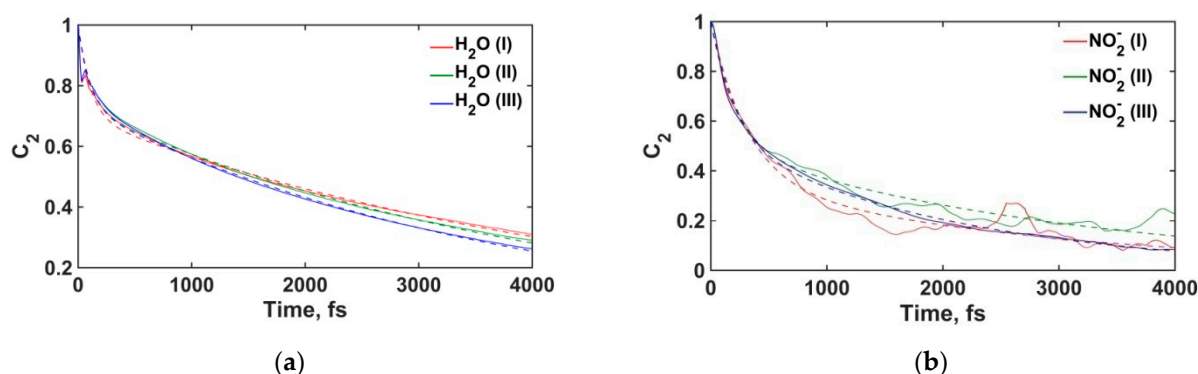
Figure 11. Time correlation functions. Dashed lines represent the biexponential fits. (**a**) H_2O molecules; (**b**) NO_2^- ions. (**I**) and (**II**) are the first and second layers of the solution, respectively. (**III**) denotes the bulk phase of the solution (see Figure 1).

Table 3. The orientational relaxation times for H_2O molecules and NO_2^-.

Molecule/Ion	Layer	τ_1, ps	τ_2, ps
H_2O	(I)	0.11	4.76
	(II)	0.11	4.21
	(III)	0.10	3.78
NO_2^-	(I)	0.32	2.89
	(II)	0.22	3.11
	(III)	0.20	2.08

The increase in τ_2 near the surface compared to their bulk solution values is seen for NO_2^- ions as well, which is also due to the participation of the nitrite ions in the more stable H-bonding network at the surface of portlandite. In the closest near-surface layer, we also observe an increase in time τ_1, indicating that the NO_2^- ion adsorption affects its libration modes.

3.2.5. Diffusional Mobility of Water and Ions at the Portlandite Surface

The translational dynamics of NO_2^-, Na^+, and H_2O molecules in the near-surface layers and in the bulk of the solution were studied by calculating the self-diffusion co-efficients of these species using the Einstein–Smoluchowski relation [41,72,73]. For H_2O molecules, we calculated the 3-dimensional (3d) diffusion coefficients separately for the solution layers (I), (II), and (III), as defined in Figure 1. For the ions, due to their relatively small number in the simulated systems, only bulk (layer (III)) 3-dimensional diffusion coefficients were calculated.

Table 4 shows the calculated self-diffusion coefficients. The average self-diffusion coefficients for the ions are found to be $D_{Na} = (0.84 \pm 0.17) \times 10^{-5}$ cm^2/s, $D_{NO_2} = (1.46 \pm 0.16) \times 10^{-5}$ cm^2/s. The calculated diffusivities of ions in water are lower than the experimental values $D_{Na}^{exp} = 1.33 \times 10^{-5}$ cm^2/s and $D_{NO_2}^{exp} = 1.91 \times 10^{-5}$ cm^2/s [74].

Table 4. Self-diffusion coefficients of ions and H_2O molecules.

Molecule/Ion	Layer	2d, 10^{-5} cm^2/s	3d, 10^{-5} cm^2/s
H_2O	(I)	0.98	1.36
	(II)	1.11	1.47
	(III)	-	1.81
Na^+	(III)	-	0.84
NO_2^-	(III)	-	1.46

The diffusional mobility of water molecules decreases as they approach the surface, with $D_{H_2O}^{III}$ = (1.81 ± 0.16) × 10^{-5} cm^2/s, $D_{H_2O}^{II}$ = (1.47 ± 0.18) × 10^{-5} cm^2/s, and $D_{H_2O}^{I}$ = (1.36 ± 0.21) × 10^{-5} cm^2/s. The diffusivity of water in the bulk layer is underestimated compared to the experimental data $D_{H_2O}^{exp}$ = 2.33 × 10^{-5} cm^2/s [75]. The reduced calculated diffusivities of water and ions reflect the effect of their interactions with the portlandite surface but are also partly due to the known underestimation of the molecular mobility by the flexible SPC/E model and due to the finite size effects of the periodic boundary conditions [76].

4. Conclusions

The recently modified ClayFF force field, ClayFF-MOH [10], with added Ca-O-H angular bending terms, together with a new parameterization for NO_2^- ions [18] were used to study the structure and dynamics of sodium nitrite solutions at the surface of portlandite using classical MD simulations. The (001) crystal surface of portlandite was selected for these simulations because it is the least reactive when interacting with water compared to other surfaces. We show that the inclusion of the Ca-O-H bending term does not affect the simulation results for the crystal structure but does affect the vibrational properties of the crystal, bringing them closer to the experimental data. This, in turn, affects the structural properties of the aqueous solutions in the near-surface layers due to the increased localization of surface hydroxyl groups of portlandite.

The better-constrained orientation of the hydroxyls on the (001) surface of portlandite leads to a more realistic description of the hydrogen bonds formed between surface hydrogen atoms and water molecules ($H_h \cdots O_w$ donor-acceptor pair), facilitating the formation of a network of H-bonds between water molecules themselves, which form a surface layer inhibiting the dissolution of calcium ions into water. The formation of the interfacial H-bonding network manifests itself in the increase in the rotational relaxation time for water molecules near the portlandite surface.

Despite the formation of the water-water H-bonding network on the surface of the crystalline phase, the surface can adsorb dissolved nitrite and sodium ions. We show that the adsorption of nitrite ions involves the formation of H-bonds donated by surface hydroxyls not only to the oxygen atoms of NO_2^-, but also to the nitrogen atoms, i.e., both $H_h \cdots O_n$ and $H_h \cdots N$ donor-acceptor pairs are present. Although the H-bonds $H_h \cdots O_n$ and $H_h \cdots N$ are weaker than the H-bonds $H_h \cdots O_w$ donated to the water molecules, NO_2^- ions infiltrate the H-bonding network on the surface of portlandite and are quite strongly adsorbed at it with no visible translational diffusion over the timescale of the entire MD simulation (~1 ns). On the other hand, the orientation of the adsorbed ions can change over time, so that there is no single preferred coordination of the adsorbed NO_2^- to the surface, meaning that the H-bonds in the $H_h \cdots O_n$ and $H_h \cdots N$ pairs are less stable and can frequently break and re-form. The NO_2^- ions can be adsorbed onto the surface of portlandite next to the previously adsorbed Na$^+$ ions as well as separately without any strong association with the cations.

Author Contributions: Conceptualization, A.G.K. and E.V.T.; methodology, A.G.K. and V.V.P.; investigation, E.V.T.; data analysis E.V.T., V.V.P. and A.G.K.; writing—original draft preparation, E.V.T.; writing—review and editing, E.V.T., V.V.P. and A.G.K.; visualization, E.V.T.; supervision, V.V.P. and A.G.K.; project administration, V.V.P. and A.G.K.; funding acquisition, E.V.T., V.V.P. and A.G.K. All authors have read and agreed to the published version of the manuscript.

Institutional Review Board Statement: Not applicable.

Informed Consent Statement: Not applicable.

Data Availability Statement: All data are available from the authors upon request.

Conflicts of Interest: The authors declare no conflict of interest.

References

1. Phair, J.W. Green chemistry for sustainable cement production and use. *Green Chem.* **2006**, *8*, 763–780. [CrossRef]
2. Rosemberg, A.M.; Gaidis, J.M. Mechanism of nitrite inhibition of chloride attack on reinforcing steel in alkaline aqueous environments. *Mater. Perform.* **2004**, *18*, 45–48.
3. Schießl, P.; Moersch, J. Effectiveness and harmlessness of calcium nitrite as a corrosion inhibitor. In Proceedings of the International RILEM Conference on the Role of Admixtures in High Performance Concrete, Monterrey, Mexico, 21–26 March 1999; RILEM Publications SARL: Paris, France, 1999; pp. 169–182.
4. Nmai, C.K. Cold weather concreting admixtures. *Cem. Concr. Compos.* **1998**, *20*, 121–128. [CrossRef]
5. Yoneyama, A.; Choi, H.; Inoue, M.; Kim, J.; Lim, M.; Sudoh, Y. Effect of a nitrite/nitrate-based accelerator on the strength development and hydrate formation in cold-weather cementitious materials. *Materials* **2021**, *14*, 1006. [CrossRef]
6. Tritthart, J.; Banfill, P.F.G. Nitrite binding in cement. *Cem. Concr. Res.* **2001**, *31*, 1093–1100. [CrossRef]
7. Vollpracht, A.; Lothenbach, B.; Snellings, R.; Haufe, J. The pore solution of blended cements: A review. *Mater. Struct.* **2015**, *49*, 3341–3367. [CrossRef]
8. Pu, Q.; Yao, Y.; Wang, L.; Shi, X.; Luo, J.; Xie, Y. The investigation of pH threshold value on the corrosion of steel reinforcement in concrete. *Comp. Concr.* **2017**, *19*, 257–262. [CrossRef]
9. Scrivener, K.L.; Kirkpatrick, R.J. Innovation in use and research on cementitious material. *Cem. Concr. Res.* **2008**, *38*, 128–136. [CrossRef]
10. Sanchez, F.; Sobolev, K. Nanotechnology in concrete—A review. *Cons. Build. Mat.* **2010**, *24*, 2060–2071. [CrossRef]
11. Mishra, R.K.; Mohamed, A.K.; Geissbühler, D.; Manzano, H.; Jamil, T.; Shahsavari, R.; Kalinichev, A.G.; Galmarini, S.; Tao, L.; Heinz, H.; et al. CemFF: A force field database for cementitious materials including validations, applications and opportunities. *Cem. Concr. Res.* **2017**, *102*, 68–89. [CrossRef]
12. Lasich, M. Sorption of natural gas in cement hydrate by Monte Carlo simulation. *Eur. Phys. J. B* **2018**, *91*, 299. [CrossRef]
13. Pellenq, R.J.M.; Kushima, A.; Shahsavari, R.; Van Vliet, K.J.; Buehler, M.J.; Yip, S.; Ulm, F.J. A realistic molecular model of cement hydrates. *Proc. Natl. Acad. Sci. USA* **2009**, *106*, 16102–16107. [CrossRef]
14. Tavakoli, D.; Tarighat, A. Molecular dynamics study on the mechanical properties of Portland cement clinker phases. *Comput. Mater. Sci.* **2016**, *119*, 65–73. [CrossRef]
15. Bahraq, A.A.; Al-Osta, M.A.; Al-Amoudi, O.S.B.; Obot, I.B.; Maslehuddin, M.; Saleh, T.A. Molecular simulation of cement-based materials and their properties. *Engineering* **2022**, *15*, 165–178. [CrossRef]
16. Cygan, R.T.; Greathouse, J.A.; Kalinichev, A.G. Advances in *clayff* molecular simulation of layered and nanoporous materials and their aqueous interfaces. *J. Phys. Chem. C* **2021**, *125*, 17573. [CrossRef]
17. Pouvreau, M.; Greathouse, J.A.; Cygan, R.T.; Kalinichev, A.G. Structure of hydrated gibbsite and brucite edge surfaces: DFT results and further development of the ClayFF classical force field with metal-O-H angle bending terms. *J. Phys. Chem. C* **2017**, *121*, 14757–14771. [CrossRef]
18. Tararushkin, E.V. Molecular dynamic modeling of the structural, dynamic, and vibrational properties of aqueous $NaNO_2$. *Russ. J. Phys. Chem.* **2022**, *96*, 1439–1444. [CrossRef]
19. Tararushkin, E.V.; Pisarev, V.V.; Kalinichev, A.G. Atomistic simulations of ettringite and its aqueous interfaces: Structure and properties revisited with the modified ClayFF force field. *Cem. Concr. Res.* **2022**, *156*, 106759. [CrossRef]
20. Kalinichev, A.G.; Kirkpatrick, R.J. Molecular dynamics modeling of chloride binding to the surfaces of calcium hydroxide, hydrated calcium aluminate, and calcium silicate phases. *Chem. Mater.* **2002**, *14*, 3539–3549. [CrossRef]
21. Cygan, R.T.; Liang, J.-J.; Kalinichev, A.G. Molecular models of hydroxide, oxyhydroxide, and clay phases and the development of a general force field. *J. Phys. Chem. B* **2004**, *108*, 1255–1266. [CrossRef]
22. Desgranges, L.; Grebille, D.; Calvarin, G.; Chhor, K.; Pommier, C.; Floquet, N.; Niepce, J.C. Structural and thermodynamic evidence of a change in thermal motion of hydrogen atoms in $Ca(OH)_2$ at low temperature. *J. Phys. Chem. Sol.* **1994**, *55*, 161–166. [CrossRef]
23. Schaack, S.; Depondt, P.; Huppert, S.; Finocchi, F. Quantum driven proton diffusion in brucite-like minerals under high pressure. *Sci. Rep.* **2020**, *10*, 8123. [CrossRef] [PubMed]
24. Busing, W.R.; Levy, H.A. Neutron diffraction study of calcium hydroxide. *J. Chem. Phys.* **1957**, *26*, 563–568. [CrossRef]
25. Galmarini, S.; Aimable, A.; Ruffray, N.; Bowen, P. Changes in portlandite morphology with solvent composition: Atomistic simulations and experiment. *Cem. Concr. Res.* **2011**, *41*, 1330–1338. [CrossRef]
26. Mutisya, S.M.; Kalinichev, A.G. Carbonation reaction mechanisms of portlandite predicted from enhanced Ab Initio molecular dynamics simulations. *Minerals* **2021**, *11*, 509. [CrossRef]

27. Harutyunyan, V.S. Adsorption energy of stoichiometric molecules and surface energy at morphologically important facets of a Ca(OH)$_2$ crystal. *Mater. Chem. Phys.* **2012**, *134*, 200–213. [CrossRef]

28. Harutyunyan, V.S. Inhomogeneity, anisotropy, and size effect in the interfacial energy of Ca(OH)$_2$ hexagonal-prism shaped nanocrystals in water. *Mat. Chem. Phys.* **2014**, *147*, 410–422. [CrossRef]

29. Salah Uddin, K.M.; Izadifar, M.; Ukrainczyk, N.; Koenders, E.; Middendorf, B. Dissolution of portlandite in pure water: Part 1 molecular dynamics (MD) approach. *Materials* **2022**, *15*, 1404. [CrossRef] [PubMed]

30. Izadifar, M.; Ukrainczyk, N.; Salah Uddin, K.M.; Middendorf, B.; Koenders, E. Dissolution of portlandite in pure water: Part 2 atomistic kinetic Monte Carlo (KMC) approach. *Materials* **2022**, *15*, 1442. [CrossRef]

31. Gardeh, M.G.; Kistanov, A.A.; Nguyen, H.; Manzano, H.; Cao, W.; Kinnunen, P. Exploring mechanisms of hydration and carbonation of MgO and Mg(OH)$_2$ in reactive magnesium oxide-based cements. *J. Phys. Chem. C* **2022**, *126*, 6196–6206. [CrossRef]

32. Aili, A.; Maruyama, I. Review of several experimental methods for characterization of micro- and nano-scale pores in cement-based material. *Int. J. Concr. Struct. Mater.* **2020**, *14*, 55. [CrossRef]

33. Berendsen, H.; Grigera, J.; Straatsma, T. The missing term in effective pair potentials. *J. Phys. Chem.* **1987**, *91*, 6269–6271. [CrossRef]

34. Vchirawongkwin, S.; Kritayakornupong, C.; Tongraarc, A.; Vchirawongkwin, V. Hydration properties determining the reactivity of nitrite in aqueous solution. *Dalton Trans.* **2014**, *43*, 12164–12174. [CrossRef]

35. Yadav, S.; Chandra, A. Solvation shell of the nitrite Ion in water: An ab initio molecular dynamics study. *J. Phys. Chem. B* **2020**, *124*, 7194–7204. [CrossRef]

36. Liu, Y.; Shi, X. Molecular dynamics study of interaction between corrosion inhibitors, nanoparticles, and other minerals in hydrated cement. *Trans. Res. Rec. J. Trans. Res. Board* **2010**, *2142*, 58–66. [CrossRef]

37. Richards, L.A.; Schäfer, A.I.; Richards, B.S.; Corry, B. The importance of dehydration in determining ion transport in narrow pores. *Small* **2012**, *8*, 1701–1709. [CrossRef]

38. Ohkubo, T.; Ohnishi, R.; Sarou-Kanian, V.; Bessada, C.; Iwadate, Y. Molecular dynamics simulations of the thermal and transport properties of molten NaNO$_2$–NaNO$_3$ systems. *Electrochemistry* **2018**, *86*, 104–108. [CrossRef]

39. Irish, D.E.; Thorpe, R.V. Raman spectral studies of cadmium–nitrite interactions in aqueous solutions and crystals. *Can. J. Chem.* **1975**, *53*, 1414–1423. [CrossRef]

40. Thompson, A.P.; Aktulga, H.M.; Berger, R.; Bolintineanu, D.S.; Brown, W.M.; Crozier, P.S.; in't Veld, P.J.; Kohlmeyer, A.; Moore, S.G.; Nguyen, T.D.; et al. LAMMPS—A flexible simulation tool for particle-based materials modeling at the atomic, meso, and continuum scales. *Comp. Phys. Comm.* **2022**, *271*, 108171. [CrossRef]

41. Allen, M.P.; Tildesley, D.J. *Computer Simulation of Liquids*, 2nd ed.; Oxford University Press: New York, NY, USA, 2017. [CrossRef]

42. Brown, W.M.; Kohlmeyer, A.; Plimpton, S.J.; Tharrington, A.N. Implementing molecular dynamics on hybrid high performance computers—Particle-particle particle-mesh. *Comp. Phys. Comm.* **2012**, *183*, 449–459. [CrossRef]

43. Brown, W.M.; Wang, P.; Plimpton, S.J.; Tharrington, A.N. Implementing molecular dynamics on hybrid high performance computers—Short range forces. *Comp. Phys. Comm.* **2011**, *182*, 898–911. [CrossRef]

44. Swope, W.C.; Andersen, H.C.; Berens, P.H.; Wilson, K.R. A computer simulation method for the calculation of equilibrium constants for the formation of physical clusters of molecules: Application to small water clusters. *J. Chem. Phys.* **1982**, *76*, 637–649. [CrossRef]

45. Nosé, S. A unified formulation of the constant temperature molecular dynamics methods. *J. Chem. Phys.* **1984**, *81*, 511–519. [CrossRef]

46. Hoover, W.G. Canonical dynamics: Equilibrium phase-space distributions. *Phys. Rev. A* **1985**, *31*, 1695–1697. [CrossRef] [PubMed]

47. Kalinichev, A.G. Atomistic modeling of clays and related nanoporous materials with ClayFF force field. In *Computational Modeling in Clay Mineralogy*; Sainz-Díaz, C.I., Ed.; Association Internationale Pour l'Etude des Argiles (AIPEA): Bari, Italy, 2021; Volume 3, pp. 17–52.

48. Henderson, D.M.; Gutowsky, H.S. A nuclear magnetic resonance determination of the hydrogen positions in Ca(OH)$_2$. *Amer. Miner.* **1962**, *47*, 1231–1251.

49. Laugesen, J.L. Density functional calculations of elastic properties of portlandite, Ca(OH)$_2$. *Cem. Concr. Res.* **2005**, *35*, 199–202. [CrossRef]

50. Ugliengo, P.; Zicovich-Wilson, C.M.; Tosoni, S.; Civalleri, B. Role of dispersive interactions in layered materials: A periodic B3LYP and B3LYP-D* study of Mg(OH)$_2$, Ca(OH)$_2$ and kaolinite. *J. Mater. Chem.* **2009**, *19*, 2564. [CrossRef]

51. Hou, D.; Lu, Z.; Zhang, P.; Ding, Q. Molecular structure and dynamics of an aqueous sodium chloride solution in nano-pores between portlandite surfaces: A molecular dynamics study. *Phys. Chem. Chem. Phys.* **2016**, *18*, 2059–2069. [CrossRef]

52. Hajilar, S.; Shafei, B. Assessment of structural, thermal, and mechanical properties of portlandite through molecular dynamics simulations. *J. Solid State Chem.* **2016**, *244*, 164–174. [CrossRef]

53. Valavi, M.; Casar, Z.; Mohamed, A.K.; Bowen, P.; Galmarini, S. Molecular dynamic simulations of cementitious systems using a newly developed force field suite ERICA FF. *Cem. Concr. Res.* **2022**, *154*, 106712. [CrossRef]

54. Sarkar, P.K.; Mitra, N. Molecular deformation response of portlandite under compressive loading. *Constr. Build. Mater.* **2021**, *274*, 122020. [CrossRef]

55. Szczerba, M.; Kuligiewicz, A.; Derkowski, A.; Gionis, V.; Chryssikos, G.D.; Kalinichev, A.G. Structure and dynamics of water-smectite interfaces: Hydrogen bonding and the origin of the sharp O-DW/O-HW infrared band from molecular simulations. *Clays Clay Min.* **2016**, *64*, 452–471. [CrossRef]

56. Lutz, H.D.; Möller, H.; Schmidt, M. Lattice vibration spectra. Part LXXXII. Brucite-type hydroxides $M(OH)_2$ (M = Ca, Mn, Co, Fe, Cd)—IR and Raman spectra, neutron diffraction of $Fe(OH)_2$. *J. Molec. Struct.* **1994**, *328*, 121–132. [CrossRef]

57. Weckler, B.; Lutz, H.D. Near-infrared spectra of M(OH)Cl (M = Ca, Cd, Sr), $Zn(OH)F$, γ-$Cd(OH)_2$, $Sr(OH)_2$, and brucite-type hydroxides $M(OH)_2$ (M = Mg, Ca, Mn, Fe, Co, Ni, Cd). *Spectr. Acta Part A Molec. Biomolec. Spectrosc.* **1996**, *52*, 1507–1513. [CrossRef]

58. Tararushkin, E.V.; Shchelokova, T.N.; Kudryavtseva, V.D. A study of strength fluctuations of Portland cement by FTIR spectroscopy. *IOP Conf. Ser. Mater. Sci. Eng.* **2020**, *919*, 022017. [CrossRef]

59. Zeitler, T.R.; Greathouse, J.A.; Gale, J.D.; Cygan, R.T. Vibrational analysis of brucite surfaces and the development of an improved force field for molecular simulation of interfaces. *J. Phys. Chem. C* **2014**, *118*, 7946–7953. [CrossRef]

60. Dupuis, R.; Dolado, J.S.; Benoit, M.; Surga, J.; Ayuela, A. Quantum nuclear dynamics of protons within layered hydroxides at high pressure. *Sci. Rep.* **2017**, *7*, 4842. [CrossRef]

61. Galmarini, S.; Bowen, P. Atomistic simulation of the adsorption of calcium and hydroxyl ions onto portlandite surfaces—Towards crystal growth mechanisms. *Cem. Concr. Res.* **2016**, *81*, 16–23. [CrossRef]

62. Stukowski, A. Visualization and analysis of atomistic simulation data with OVITO–the Open Visualization Tool. *Model. Simul. Mater. Sci. Eng.* **2009**, *18*, 015012. [CrossRef]

63. Hu, X.; Zheng, H.; Tao, R.; Wang, P. Migration of nitrite corrosion inhibitor in calcium silicate hydrate nanopore: A molecular dynamics simulation study. *Front. Mater.* **2022**, *9*, 965772. [CrossRef]

64. Maréchal, Y. IR spectroscopy of an exceptional H-bonded liquid: Water. *J. Molec. Struct.* **1994**, *322*, 105–111. [CrossRef]

65. Tominaga, Y.; Fujiwara, A.; Amo, Y. Dynamical structure of water by Raman spectroscopy. *Fluid Phase Equilibria* **1998**, *144*, 323–330. [CrossRef]

66. Antipova, M.L.; Petrenko, V.E. Hydrogen bond lifetime for water in classic and quantum molecular dynamics. *Russ. J. Phys. Chem.* **2013**, *87*, 1170–1174. [CrossRef]

67. Rapaport, D.C. Hydrogen bonds in water. *Mol. Phys.* **1983**, *50*, 1151–1162. [CrossRef]

68. Chanda, J.; Bandyopadhyay, S. Hydrogen bond lifetime dynamics at the interface of a surfactant monolayer. *J. Phys. Chem. B* **2006**, *110*, 23443–23449. [CrossRef] [PubMed]

69. Chowdhuri, S.; Chandra, A. Hydrogen bonds in aqueous electrolyte solutions: Statistics and dynamics based on both geometric and energetic criteria. *Phys. Rev. E.* **2002**, *66*, 041203. [CrossRef] [PubMed]

70. Laage, D.; Hynes, J.T. A Molecular jump mechanism of water reorientation. *Science* **2006**, *311*, 832. [CrossRef]

71. Laage, D.; Stirnemann, G.; Sterpone, F.; Rey, R.; Hynes, J.T. Reorientation and allied dynamics in water and aqueous solutions. *Annu. Rev. Phys. Chem.* **2011**, *62*, 395–416. [CrossRef]

72. Mutisya, S.M.; Kirch, A.; de Almeida, J.M.; Sánchez, V.M.; Miranda, C.R. Molecular dynamics simulations of water confined in calcite slit pores: An NMR spin relaxation and hydrogen bond analysis. *J. Phys. Chem. C* **2017**, *121*, 6674–6684. [CrossRef]

73. Kondratyuk, N.D.; Norman, G.E.; Stegailov, V.V. Self-consistent molecular dynamics calculation of diffusion in higher *n*-alkanes. *J. Chem. Phys.* **2016**, *145*, 204504. [CrossRef]

74. Lide, D.R. *CRC Handbook of Chemistry and Physics*, 84th ed.; CRC Press: Boca Raton, FL, USA, 2004.

75. Krynicki, K.; Green, C.D.; Sawyer, D.W. Pressure and temperature dependence of self-diffusion in water. *Faraday Discuss. Chem. Soc.* **1978**, *66*, 199–208. [CrossRef]

76. Celebi, A.T.; Jamali, S.H.; Bardow, A.; Vlugt, T.J.H.; Moultos, O.A. Finite-size effects of diffusion coefficients computed from molecular dynamics: A review of what we have learned so far. *Molec. Simul.* **2020**, *47*, 831–845. [CrossRef]

77. Kostenetskiy, P.S.; Chulkevich, R.A.; Kozyrev, V.I. HPC Resources of the Higher School of Economics. *J. Phys. Conf. Ser.* **2021**, *1740*, 012050. [CrossRef]

78. Kostenetskiy, P.; Shamsutdinov, A.; Chulkevich, R.; Kozyrev, V.; Antonov, D. HPC TaskMaster—Task efficiency monitoring system for the supercomputer center. In Proceedings of the International Conference on Parallel Computational Technologies, Dubna, Russia, 29–31 March 2022; Volume 1618, pp. 17–29. [CrossRef]